

Article

Effects of Processing Conditions on the Properties of Porous Diatomite Granules Prepared by Sodium Alginate Gelation

Maria Dolores Sosa Lucio ^{1,2}, Eun-Ji Oh ¹, Jang-Hoon Ha ^{1,*}, Jongman Lee ^{1,2} , Hong-Joo Lee ¹
and In-Hyuck Song ^{1,2} 

¹ Ceramic Materials Division, Korea Institute of Materials Science (KIMS), 797 Changwon-daero, Seongsan-gu, Changwon-si 51508, Republic of Korea; mariasosa@kims.re.kr (M.D.S.L.); hey22@kims.re.kr (E.-J.O.); jmlee@kims.re.kr (J.L.); hjlee@kims.re.kr (H.-J.L.); sih1654@kims.re.kr (I.-H.S.)

² Department of Advanced Materials Engineering, University of Science and Technology (UST), 217 Gajeong-ro, Yuseong-gu, Daejeon 34113, Republic of Korea

* Correspondence: hjhoon@kims.re.kr

Featured Application: Porous ceramic supports, and catalytic ceramic carrier.

Abstract: The proper application of millimeter-sized spherical porous ceramic supports in catalytic operations relies on their ease of handling, convenient separation, recyclability, high-catalyst-solid loading, and the optimum mass transfer of reactants and products. However, common granulation techniques of spherical carriers entail complex liquid-phase-based processes under severe conditions and the use of toxic or expensive reagents. The present study discusses the manufacturing of porous ceramic granules derived from an inexpensive silica source (diatomite, solid network) and a biopolymer cross-linked by ion exchange (sodium alginate, patterning structure). The results indicated that, with fixed granulation conditions, porous diatomite granules with a sphericity of approximately 0.9 could be successfully obtained by optimization of the diatomite/sodium alginate dispersion to a 30.07 wt.% solid content and 1560 mPa·s viscosity (at $\sim 0.3 \text{ s}^{-1}$). Moreover, the described manufacturing process was proven effective in developing hierarchically porous diatomite granules that were heat-treated at 1200 °C with high sphericity (~ 0.9), acceptable compressive strength ($5.17 \pm 0.31 \text{ MPa}$), and porosity features (total porosity: $69.0 \pm 2.9\%$, macropore size: $2.777 \mu\text{m}$, mesopore size: 35.34 nm), establishing them as well-matched support materials for either catalytic or adsorption applications.

Keywords: porous diatomite granules; sodium alginate gelation; sphericity; porosity; pore size; compressive strength



Citation: Sosa Lucio, M.D.; Oh, E.-J.; Ha, J.-H.; Lee, J.; Lee, H.-J.; Song, I.-H. Effects of Processing Conditions on the Properties of Porous Diatomite Granules Prepared by Sodium Alginate Gelation. *Appl. Sci.* **2023**, *13*, 9474. <https://doi.org/10.3390/app13169474>

Academic Editor: Aliaksandr Shaula

Received: 28 July 2023

Revised: 16 August 2023

Accepted: 16 August 2023

Published: 21 August 2023



Copyright: © 2023 by the authors. Licensee MDPI, Basel, Switzerland. This article is an open access article distributed under the terms and conditions of the Creative Commons Attribution (CC BY) license (<https://creativecommons.org/licenses/by/4.0/>).

1. Introduction

Porous ceramic supports have attracted significant attention with regard to filtration, absorption, and catalytic applications due to certain intrinsic properties, such as their remarkable hardness and strength, low-thermal-expansion coefficient, stability at high temperatures, and good wear and corrosion resistance. Additionally, they exhibit notable extrinsic properties, including a low-density level, controlled permeability, tailored thermal conductivity, and a high specific surface area [1–5]. Particularly, a sizeable specific surface area, uniform particle size, narrow pore size distribution and volume, good chemical and thermal stability, and high-mechanical strength are highly desirable to ensure good performance of porous ceramic supports in catalytic applications [2,4]. The morphology of the support, the processing route, and the raw starting material significantly influence the tailoring of the aforementioned properties of the supports.

Supports or ceramic carriers in a powdered form (ranging from nano- to micron-sized particles) have limitations in large-scale applications due to the difficulties in material handling, separation from the process fluids, environmental release, and contamination [2,6–8].

Porous materials on the macroscopic scale, specifically millimeter-sized ceramic supports, are considered suitable carrier options that offer ease of handling, high-catalyst-loading percentages within equivalent reactor volumes, high-efficiency levels, good stability, convenient recovery, proper separation, and recyclability after a heterogeneous reaction process [7–9], while promoting high mass transfer rates [2,10]. Moreover, it has been suggested that ceramic beads with a spherical shape (sphericity ~ 1 , sphericity factor ~ 0) significantly reduce resistance to the transport of reactants and products, as well as catalyst abrasion, compared to non-spherical or irregularly shaped granules [6,11,12].

Common liquid-phase-based techniques for processing spherical ceramic carriers, depending on the sol's congealing route, include the granulation methods known as "oil-molding" and "hydrocarbon-ammonia molding" [13,14]. These techniques, referred to as "internal gelation" and "external gelation", respectively, are sol-gel processes used in the fabrication of nuclear fuel kernels [15].

In the oil-molding route, the starting broth, a dispersion of precursors (with controlled acidity) and a gelling agent such as hexamethylenetetramine (HMTA) or a mixture of HMTA and urea (organic monomer) [3,15], is introduced dropwise into hot oil ($\sim 90^\circ\text{C}$), resulting in the generation of gel droplets due to surface tension as they enter the oil bath [3,16]. The sol congeals through neutralization with ammonia ions upon the decomposition of the HMTA and/or urea, while the droplets age in the hot oil [3,13]. Finally, spherical ceramic carriers are obtained after washing filtration (using organic solvents, ammonia solution, and deionized water), drying, and a heat treatment [3,13,15]. The oil molding route has been primarily used to prepare $\gamma\text{-Al}_2\text{O}_3$ spherical granules [3,16–18] and CeO_2 -stabilized- ZrO_2 (CSZ) [15], $\text{Al}_2\text{O}_3\text{-CeO}_2$ [19], Y_2O_3 -stabilized ZrO_2 [20], and $\text{CeO}_2\text{-Nd}_2\text{O}_3$ [21] fuel kernels and pellets (referred to as internal gelation). Despite the achieved uniformity of the processed spheres, major drawbacks of this method include the toxic nature of the reagents, the requirements of the use and disposal of hot oil together with by-products, and the necessity to maintain the granules under severe processing conditions to complete the decomposition of HMTA and urea [13].

The hydrocarbon-ammonia route entails a series of stages, including the preparation of a precursor-derived hydroxide gel, the formation of a pseudosol through the treatment of the hydroxide (or hydrated precursor [22]) by a peptizer acid, granulation, washing filtration, drying, and a heat treatment [4,13,23]. For the granulation step, the pseudosol broth is transferred dropwise into a gelation column consisting of a liquid hydrocarbon (oil) on the top and an ammonia solution (gelling media) at the bottom. The sol drops are formed due to surface tension when they come into contact with the superficial oil layer and are subsequently congealed in the coagulant ammonia solution [3,13,15]. Examples of this route mainly include $\gamma\text{-Al}_2\text{O}_3$ [6,12,24], $\text{TiO}_2/\gamma\text{-Al}_2\text{O}_3$ [25], N-doped $\text{TiO}_2/\gamma\text{-Al}_2\text{O}_3$ [26], and silicate/ $\gamma\text{-Al}_2\text{O}_3$ -derived granules [4], as well as CSZ [15,22] and ZrO_2 fuel kernels and pellets (referred to as external gelation) [27]. However, the cost of the precursors for the initial broth and the toxic-corrosiveness of the gelling bath are negative aspects to be considered when using this route for industrial purposes [3].

Given the complexity and drawbacks of the aforementioned processes, alternative routes are needed to achieve the required properties for optimal performance of the millimeter-sized spherical porous ceramics while minimizing the impact of the experimental conditions. Building upon the concept of "integrative chemistry" introduced by Backov [28], Prouzet et al. [29] proposed an innovative approach termed "integrated gelling", which involves the simultaneous gelation of both an inorganic framework (raw material) and a biopolymer by the sol-gel process and ion exchange-crosslinking, respectively. Based on this strategy, Prouzet et al. [29] prepared millimeter-sized granules from a sodium alginate/boehmite suspension, followed by calcination to provide porous $\gamma\text{-Al}_2\text{O}_3$ beads.

Sodium alginate, a natural biopolymer extracted from seaweed [29,30], is widely recognized for its use as gelling, emulsifying, and viscosifying additive in the food industry. It also finds applications in biomedical fields, such as for protein or cell encapsulation, drug delivery, and tissue engineering [29–31]. Sodium alginate is an ionic linear un-

branched chain consisting of polysaccharides, specifically β -(1–4)-D-mannuronic acid (M) and α -(1–4)-L-guluronic acid (G) [30]. These units are arranged along the chain such that they form distinct sections of polymannurate (M block), polyguluronate (G block), and alternating G and M regions (MG block) [30,31]. The carboxyl group (COO^-) present in the monomer sections is bound to Na^+ . The cross-linking property of the sodium alginate chain is essential in the integrated gelling method. In the presence of multivalent ions, such as Ca^{2+} , Ba^{2+} , Sr^{2+} , Al^{3+} , La^{3+} , and others [32], the Na^+ cations undergo ion exchange, resulting in the binding of functional monomers in the chain through COO^- groups [29,33]. Notably, the binding between G blocks (junction zones) is more pronounced, particularly when divalent ions such as Ca^{2+} , Ba^{2+} , and Sr^{2+} are utilized. This results in the formation of structures commonly known as egg-box dimers [31,32,34]. Among these ions, the use of a Ca^{2+} (aq) gelling bath is particularly highlighted due to its non-toxicity, biocompatibility, and ability to produce strong alginate-derived gels [32,35]. Consequently, the integrated gelling method, based on the cross-linking of sodium alginate with a Ca^{2+} (aq) gelling bath, constitutes a versatile patterning and encapsulation technique of solid networks. However, there is limited research on the effects of the processing conditions of this method on the synthesis of millimeter-sized spherical porous ceramic supports [11]. Therefore, it is important to explore applications of comparable examples of this route in the synthesis of alternative spherical porous ceramic supports and study their resultant properties.

Porous ceramic supports with hierarchical pore systems (macro-, meso-, and/or micropores) within their solid networks have garnered increasing interest due to the combined structural stability and functionality offered by these features [2,5]. Diatomite, also known as diatomaceous earth, is a lightweight fine-grained biogenic sediment with a unique set of properties that has gained attention in both the industrial and academic fields as a suitable raw material for certain applications, including filters, absorbers, catalytic supports, and fillers [36,37]. Diatomite is derived from the frustules of diatoms, which are fossilized unicellular algae or microscopic plants. These frustules primarily consist of amorphous hydrated silica ($\text{SiO}_2 \cdot n\text{H}_2\text{O}$), which is categorized as a non-crystalline opal-A [36,38]. With dimensions in the range of 1–100 μm (usually $>10 \mu\text{m}$, depending on the species), diatomite frustules display distinctive bimodal meso/macroporosity [38,39], which influences the specific surface area and facilitates efficient mass-transport and diffusion processes [38]. Additionally, diatomite exhibits strong acid resistance, thermal stability, low-thermal conductivity, and high-mechanical strength, making it highly desirable for the aforementioned applications [36,38]. Moreover, diatomite is an inexpensive, easily available, and abundant form of silica [36,37].

To the best of the authors' knowledge, no previous report has focused on the preparation and optimization of millimeter-sized spherical porous diatomite supports (hereafter referred as porous diatomite granules) based on the "integrated gelling" approach [29]. Additionally, there is a lack of research on the effects of heat-treatment conditions on the pore and mechanical characteristics of these granules. Therefore, this study aims to propose the preparation of an alternative porous ceramic carrier, with potential applicability as a catalytic support using a low-cost and abundant raw material along with a processing route that involves non-toxic reactants. Specifically, the suggested method entails the use of diatomite/sodium alginate dispersions and the gelling of sodium alginate by cross-linking with Ca^{2+} cations as the gelling agent (physical cross-linking) [30].

2. Materials and Methods

In this study, diatomite powder (flux calcined, Celite 499, Celite Corp, Lompoc, CA, USA, 92.0% SiO_2 as referred to in Table 1) and sodium alginate (Daejung Chemicals and Metals, Gyeonggi-do, Republic of Korea) were used as raw materials for the preparation of porous diatomite granules. The manufacturing process of the porous diatomite granules was a dropwise granulation process, which was described in previous works [6,11,40]. Diatomite-based slurries were prepared by ball-milling (5 mm-sized alumina balls, 200 rpm, 4 h) different amounts of powders, ranging from 4 to 44 g (diatomite solid content: 3.8 to

30.5 wt.%) in 100 mL of distilled water (DI water) with the addition of 1 wt.% of Dolapix CE64 (Zschimmer and Schwarz Chemie GmbH, Lahnstein, Germany) as a dispersant. The compositions were designated as “DX”, where “D” represents diatomite and “X” denotes the mass of the diatomite used to prepare the batches (Figure S1). Subsequently, diatomite/sodium alginate dispersions were obtained by mixing the diatomite slurries with a fixed content of 1.5 wt.% of sodium alginate. The mixing process was carried out for 4 h at 300 rpm, followed by overnight stirring at 200 rpm to de-foam the gels. The sodium alginate content was fixed considering the minimum concentration required to achieve high sphericity (sphericity ~ 1 , sphericity factor ~ 0), as reported in previous studies of sodium alginate droplet gelation [40,41]. The resulting dispersions were transferred dropwise through a syringe tip with a diameter of 1 mm into a column containing a 10 wt.% CaCl_2 solution (aq) (Daejung Chemicals and Metals, Gyeonggi-do, Republic of Korea). The collection distance between the syringe tip and the surface of the CaCl_2 bath was set to 1 cm. The wet-gel droplets were allowed to age for 1 h in the CaCl_2 solution, after which they were separated by simple filtration and washed with DI water. The resulting granules were dried at 80 °C overnight and subsequently heat-treated at 1200 °C for 1 h in air. The granules obtained with a selected batch composition (sphericity ~ 1 , sphericity factor ~ 0) were heat-treated at different temperatures, in this case, 900 °C, 1000 °C, and 1100 °C. Granules derived from the selected processing conditions were labeled as “DX-Y”, where “D” represents diatomite, “X” denotes the mass of the diatomite used to prepare the dispersion, and “Y” represents the first one or two digits of the heat-treatment temperature. In this case, “0” refers to dried granules, i.e., green body, “9” refers to 900 °C, “10” refers to 1000 °C, and so on. A diagram illustrating the different processing steps is provided in Figure 1. Specific resulting properties of the materials, dispersions, and porous diatomite granules were characterized throughout the manufacturing process.

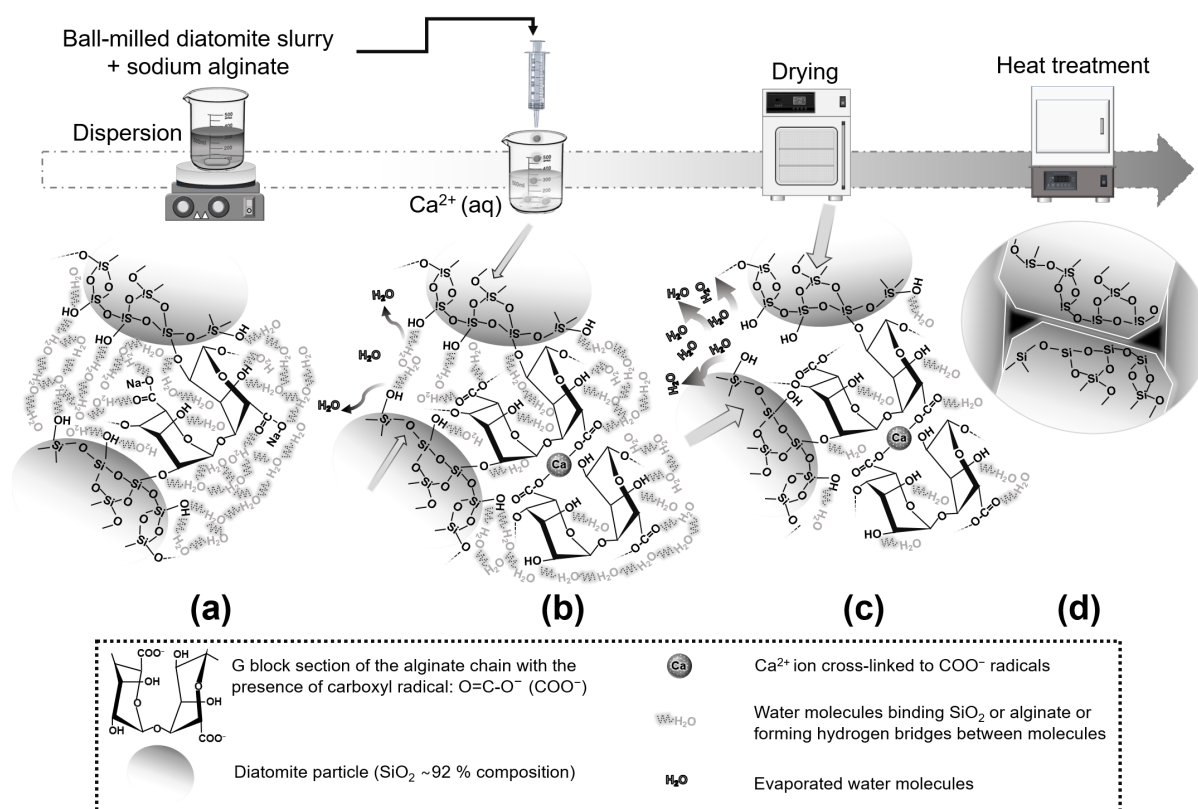


Figure 1. Diagram of the steps and mechanisms involved in the processing of porous diatomite granules, including (a) preparation of the diatomite/sodium alginate dispersion, (b) gelation of dispersion droplets in a Ca^{2+} bath, (c) evaporation of encapsulated water through drying, and (d) bonding of diatomite particles after a heat treatment.

The average particle size distributions of the processing powders were determined using a particle size analyzer (LSTM 13 320 MW, Beckman Coulter, Brea, CA, USA). The viscosity curves of the diatomite/sodium alginate dispersions were measured using a rotary viscometer (ViscoQC300, Anton Paar GmbH, Graz, Austria). The quantitative measure of the granule shape was calculated according to the sphericity, as described in the literature [6,42].

The bulk density (ρ_b) of the granules was determined according to the ISO 18754 standard [43] with the following equation:

$$\rho_b = m_1 \times \rho_1 / (m_3 - m_2), \quad (1)$$

where m_1 , m_2 , m_3 , and ρ_1 are the weight of a dried specimen (one particle), weight of a specimen submerged in water, weight of a specimen saturated with water, and the density of water at 25 °C ($\sim 1.0 \text{ g/cm}^3$), respectively. The porosities of the specimens were calculated based on the bulk densities of the specimens and the theoretical density of diatomite (ρ_{th} : 2.30 g/cm^3), according to the following equation [44]:

$$\text{Porosity (\%)} = (1 - \rho_b / \rho_{th}) \times 100 \quad (2)$$

The pore size distribution was assessed by means of mercury porosimetry (Autopore IV 9510, Micromeritics, Norcross, GA, USA). N_2 adsorption/desorption isotherms at the liquid nitrogen temperature (77 K) were measured utilizing a Belsorp-max II system (MicrotracBEL Corp., Osaka, Japan). The specific surface areas were calculated from the linear part of the adsorption data using the Brunauer–Emmett–Teller (BET) method. All the specimens were degassed at 150 °C under vacuum conditions for 8 h to ensure the detection of the pressure gradient. The total pore volume was determined at a relative pressure level of $p/p_0 = 0.99$ [6]. The fracture force (F_B), which represents the maximum load applied to break an individual granule [3], was measured using a compression tester machine (DU-B-004, DUE tester CO., Gyeonggi, Republic of Korea). The compressive strengths of the granules were calculated from F_B values considering the dimensions of the tested granules (radius: R) [3]:

$$\text{Compressive strength} = F_B / \pi R^2 \quad (3)$$

The phase analysis of the granules was conducted using an X-ray diffractometer (D/Max 2500 V/PC, Rigaku Corporation, Akishima, Japan) with $\text{Cu K}\alpha$ radiation generated at 40 kV and 200 mA and a scanning speed of $5^\circ/\text{min}$. Cross-sectioned microstructures and surface morphologies of the particles were observed with a scanning electron microscope (SEM, JSM-5800, JEOL, Tokyo, Japan).

Table 1. Typical chemical analysis results of diatomite (%).

SiO_2 *	Al_2O_3	Fe_2O_3	CaO	MgO	$\text{Na}_2\text{O} + \text{K}_2\text{O}$	Loss of Ignition (1000 °C)
92.0	1.0	1.5	0.3	0.3	2.5	0.2

* Up to 72.5% of crystalline phase (<70.0% cristobalite, <2.5% quartz).

3. Results

3.1. Characterization of Diatomite Powders, Diatomite/Sodium Alginate Dispersions and Resultant Granules

The particle size distributions of the diatomite powders with a major SiO_2 composition, as shown in Table 1, were compared before (as-received diatomite) and after ball-milling for four hours, as presented in Figure 2. The results indicate that the average particle size of the diatomite powders decreased from 13.92–14.25 μm (average particle size: $\sim 13.96 \mu\text{m}$, D_{10} : 5.57 μm , D_{50} : 11.14 μm) for the as-received-diatomite to 5.48–5.77 μm (D_{10} : 0.26 μm ,

D_{50} : 5.42 μm) for the ball-milled diatomite powders. The ball-milling process resulted in a narrowed particle size distribution and increased uniformity of the diatomite particles by reducing agglomerates [45,46]. According to the literature, this improved particle size distribution is beneficial for optimizing the viscosity of processing dispersions [46] and for enhancing the mechanical strength of the resultant ceramics [45] due to the formation of ordered particle domains. The described trends were observed in our previous studies of reticulated porous ZrO_2 and ZrO_2 -toughened Al_2O_3 ceramics [47,48], where ball-milling enabled the tailoring of the particle size distribution of the raw materials, resulting in the optimized viscosity of the processing slurries and improved compressive strength capabilities of the ceramic materials.

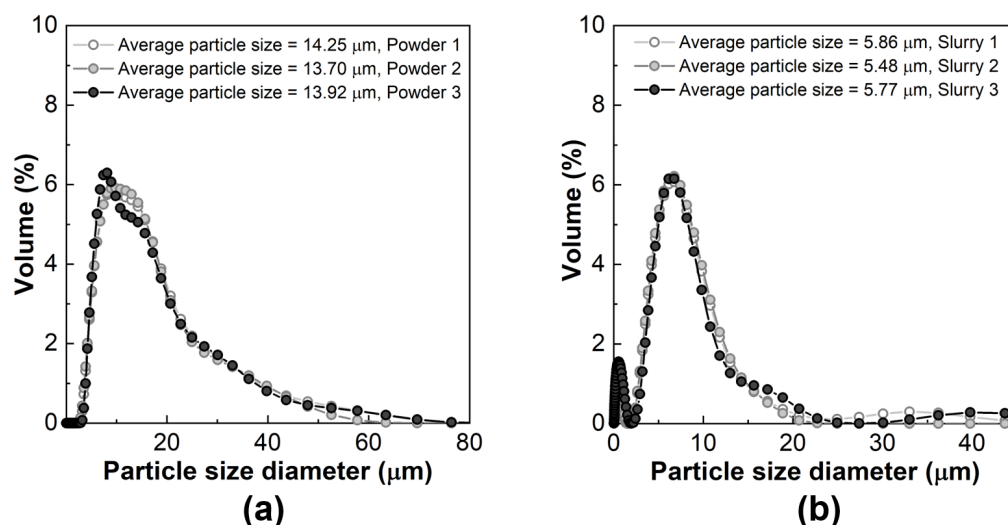


Figure 2. Particle size distributions of three different samples in each case: (a) as-received diatomite powders and (b) diatomite powders after ball-milling for 4 h.

Furthermore, the ball-milled diatomite powders exhibited a bimodal particle size distribution (average particle size: $\sim 5.70 \mu\text{m}$), which resulted from the breakup of large diatomite particles originating two maximum values of modes, a primary peak at around D_{50} : 5.35–5.47 μm and a secondary peak at around 0.31–0.54 μm , corresponding to the D_{10} value of the distribution ($\sim 0.26 \mu\text{m}$). Earlier works focusing on Al_2O_3 ceramic materials found that bimodal particle size distributions of Al_2O_3 with a smaller fraction (10–30%) of finer particles can enhance the packing density, i.e., the bulk density of the green body, in systems with a fixed solid content. This fraction of finer particles promoted the optimization of the viscosity of the processed slurries and enhanced the inter-particle bonding by filling the gaps between the grains, resulting in improved mechanical properties [49,50].

Based on the analysis above, it is proposed that the applied milling processing conditions, as determined from our previous research (4 h, 200 rpm) [37], which prevent the pulverization of the diatomite frustules, are likely to improve the regularity of the particle size distribution of the diatomite powders. Consequently, the use of ball-milled diatomite powders is expected to optimize the properties of the diatomite/sodium alginate dispersions and porous diatomite granules, compared to using as-received diatomite powders without prior processing.

Figure 3 presents the viscosity of diatomite/sodium alginate dispersions prepared with diatomite contents ranging from 3.8 to 30.5 wt.% (D04–D44) as a function of the shear rate (Figure 3a) and rpm (Figure 3b). The suspensions of diatomite and sodium alginate are created by mixing the milled diatomite slurries and sodium alginate at a fixed content to ensure the homogeneity of the mixture. As depicted in the diagram in Figure 1a, a SiO_2 /sodium alginate dispersion (diatomite: 92% SiO_2) was formed through non-covalent bonds, in this case, hydrogen bonds and van der Waals interactions between the silanol groups (SiOH) in the SiO_2 and the polar groups (OH^- and COO^-) of the sodium alginate [51,52]. Additionally,

hydrogen bonds form between the superficial silanol from SiO₂ and the water molecules in the suspensions [51,52]. Likewise, hydrogen bonds exist between the water molecules and polar groups (OH- and COO-) along the sodium alginate chains [53]. It is worth noting that, initially, both SiO₂ particles (pka~2) [54] and sodium alginate particles (pka~3–4) display significant dispersibility in water above their respective pka values [55]. However, diatomite/sodium alginate–water system consists of powders suspended in water where aggregation of these particles arises due to inter-particle attractive forces, such as van der Waals interactions, especially pronounced among the SiO₂ particles due to their higher concentration [56,57]. In this context, the application of the dispersing agent Dolapix CE 64 promotes the electrostatic stabilization of the particles. Dolapix CE 64 features a COO- functional group that dissociates in water, becoming negatively charged and adsorbed onto the surface of SiO₂ particles. This results in electrostatic repulsion between SiO₂ particles in the suspension [47,57], effectively mitigating their aggregation.

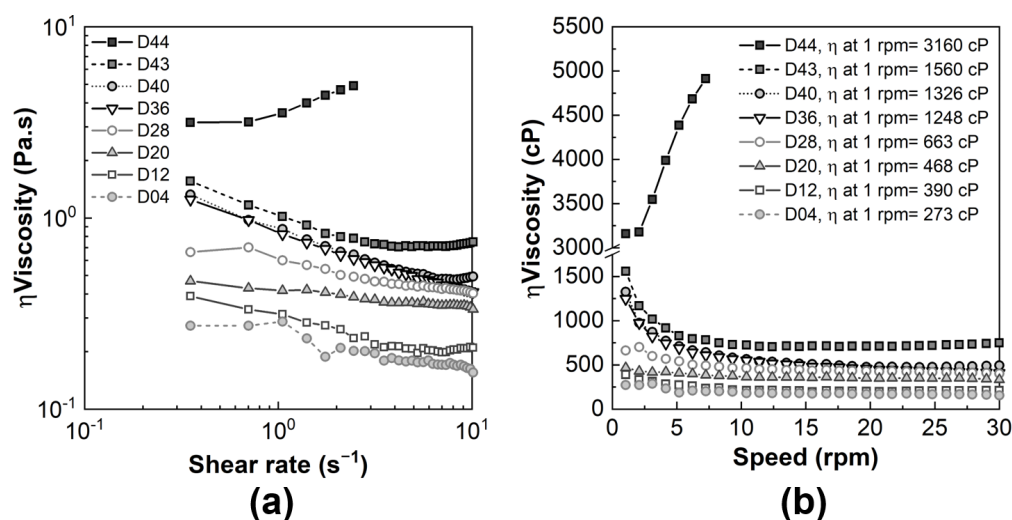


Figure 3. Viscosity values of different diatomite/sodium alginate dispersions as a function of the (a) shear rate and (b) rpm (viscosities at 1 rpm included in the figure).

The viscosity of the D04 to D43 dispersions primarily exhibited shear-thinning behavior with an increasing shear rate. However, for dispersions with higher diatomite contents (D40 and D43), this trend shifted slightly. Specifically, the D43 dispersion showed a transition from shear-thinning behavior (0.35 1/s to 3.52 1/s) towards an equilibrium state (3.85 1/s to 7.33 1/s), followed by a shear-thickening phase (7.71 1/s to 10.14 1/s). Additionally, the D44 dispersion exhibited a gradual shift from a nearly stagnant state (0.35 1/s to 0.70 1/s) to shear-thickening behavior (1.05 1/s to 2.45 1/s).

These outcomes are attributable to the interplay of various forces. At low shear rates, suspended SiO₂ particles are subject to repulsive inter-particle electrostatic forces, which stabilize the diatomite/sodium alginate dispersion and maintain a shear-thinning state [58]. However, shear-thickening behavior arises due to strong hydrodynamic interactions between SiO₂ particles as the shear rates increase, resulting in the formation of hydroclusters (coupled particles) [59]. These hydroclusters hinder the flow of particles around each other under high-flow conditions, leading to higher energy dissipation and a sudden increase in the viscosity [59].

For the case of D44 dispersion, the viscosity values could not be determined beyond 7.25 rpm due to the viscosity exceeding the limit of the viscometer, under identical experimental conditions. The higher diatomite solid content in the D44 dispersion formulation increased the number of SiO₂ particles, resulting in enhanced hydrodynamic forces and shorter distances between the particles. This, in turn, led to the formation of a larger number of hydroclusters at lower shear rates, resulting in increased motion resistance and viscosity with higher shear rates up to a certain threshold [59,60].

Representative diatomite-sodium alginate granules (D44, D43, D12, and D04) obtained at each step of the processing route are presented in Figure 4 (Additional images are presented in Figures S2 and S3 in the Supplementary Materials). The diatomite-derived porous granules were obtained by dripping droplets from the diatomite/sodium alginate dispersions into a gelling bath of CaCl_2 , as shown in Figure 1. The process begins with liquid droplets that are detached from the capillary, initially having a tear-like shape. During the granulation-falling process, these droplets evolve into an egg-like shape (ellipsoid) before eventually assuming a spherical shape due to the surface tension effect [40,41]. When considering specific granulation conditions, the ability to maintain a consistent shape during the process of droplet granulation and falling is likely determined by the properties of the diatomite/sodium alginate dispersion, particularly the viscous forces exerted by the fluid [40,41]. Upon contact between the sodium alginate in the liquid droplets and the Ca^{2+} cations in the gelling bath, localized cross-linking rapidly initiates on the droplet surface, forming an external primary membrane. This was facilitated by the rapid gelation kinetics in the ion exchange process between Na^+ ions interacting with the COO^- units of sodium alginate and Ca^{2+} ions in the gelling bath [11]. Each Ca^{2+} cation bound to four guluronate monomers [30–33], leaving encapsulated water, SiO_2 particles interacting with the monomer units of sodium alginate [61], and the remaining sodium alginate chains towards the core of the droplets. Subsequent layers of sodium alginate chains became cross-linked through the continuous inward diffusion of Ca^{2+} (aging process), promoting homogeneous gelation [11,62], particularly at high gelling bath concentrations (minimum 0.3–2 wt.% CaCl_2 [11,40]). Additionally, the particles were brought closer together during the gelling process, reducing the inter-particle space and the mass of bound water (Figure 1b) [11].

In previous studies, the extent of the ion exchange equilibrium between Na^+ and Ca^{2+} was qualified by the degree of substitution, which is related to the interactions between COO^- groups and Ca^{2+} cations forming COOCa units over the crosslinking period (immersion time in CaCl_2 bath). Research conducted with sodium alginate films (prepared from a casting solution of 1.76 wt.% sodium alginate) cross-linked using a 0.55 wt.% CaCl_2 solution revealed that the degree of substitution reached a plateau after 10 min of cross-linking. This indicated a constant presence of COOCa units, leaving approximately 10% of sodium ions unreplaced while maintaining a constant concentration of Ca^{2+} cations in the bath [33]. Moreover, it is suggested that the initial stages of the gelation are accelerated by the accessibility of the alginate chains to Ca^{2+} cations. It is important to note that extended aging times (ranging from 30 min to 12 h) were employed to ensure the hardening and proper handling of the resulting granules, depending on the experimental conditions [11,34,40].

After undergoing the aging and cleaning processes (Figure 4a), the resulting gel granules from the D04 and D44 dispersions exhibited distinct shapes with tear-like and pear-like characteristics, respectively. As the diatomite solid content in the dispersions increased (i.e., higher viscosity), the gel granules transitioned from tear-like (D04) to egg-like shapes (D08–D40,) and eventually approached a more spherical shape in the case of the D43 dispersion. However, during the subsequent processing steps, the final shape of the granules was slightly modified. This was observed when examining the D12 specimens, which appeared as ellipsoid-shaped granules with a small protrusion after the drying and heat treatment processes (Figure 4b,c), despite the absence of the protrusion in the gel state (Figure 4a). Specifically, after drying, the shrinkage percentages were higher for the D04 to D16 granules (ranging from 59.6% to 45.0%) compared to those of granules derived from dispersions with higher solid contents (D40 to D44), which experienced lower shrinkage percentages (ranging from 25.8% to 4.6%). This phenomenon can be explained as follows: (1) Assuming a fixed tip dimension of 1 mm, we can consider a comparable volume of droplets (diatomite/sodium alginate dispersion) being detached from the capillary. (2) During the flow of the dispersion through the tip, the suspended SiO_2 particles were concentrated in the tip and were redistributed within the droplet as it is ejected. In particular, a significant concentration of particles tends to localize in the

area/volume of the droplet that was lastly detached from the tip [63]. (3) With the increase in the diatomite content in the dispersion, more SiO_2 particles become bound to sodium alginate within the droplet. As a result, the area/volume occupied by these particles increases, leading to a decrease in the area/volume occupied by bound water within the droplet. (4) Eventually, the cross-linked alginate chains encapsulate the SiO_2 particles, following their distribution pattern within the droplet.

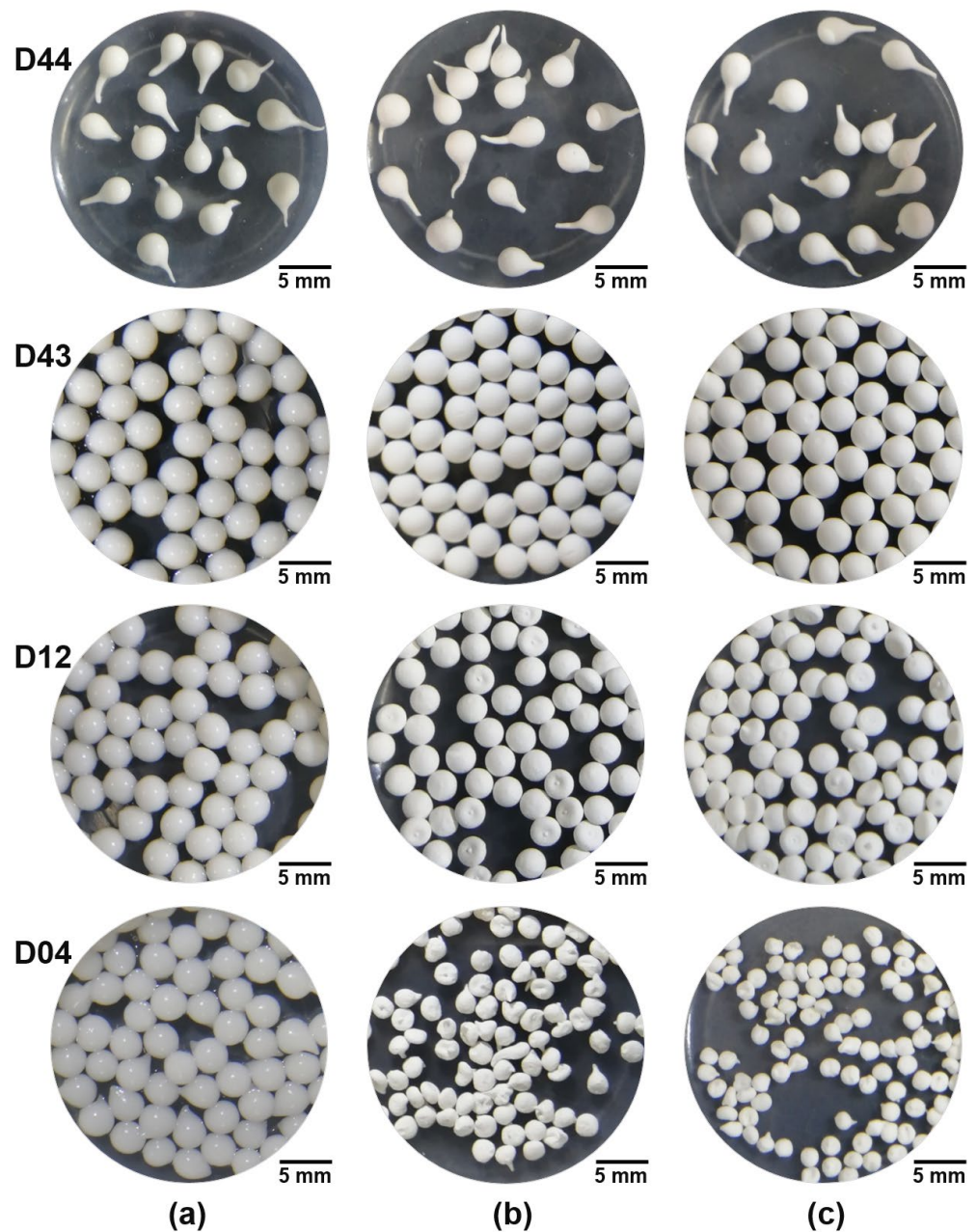


Figure 4. Representative porous diatomite granules (D44, D43, D12, and D04) obtained after each step in the processing route: (a) aging (CaCl_2 bath) and cleaning (DI water), (b) drying ($80\text{ }^\circ\text{C}$, overnight), and (c) a heat treatment at $1200\text{ }^\circ\text{C}$ for 1 h in air. (Additional images corresponding to porous diatomite granules between D08–D24 and D28–D40 are presented in Figures S2 and S3 in the Supplementary Materials).

It is suggested that, for low diatomite contents (D04 to D16), there were fewer binding sites between SiO_2 and sodium alginate, leading to the formation of more hydrogen bonds between sodium alginate and water. Likewise, the hydrophilicity of the SiO_2 particles in

the formulated dispersions facilitated the formation of hydrogen bonds. Consequently, the volume of bound water present in the droplets was higher, resulting in lower viscosity compared to that of the D43 dispersion. For higher solid contents (D20 to D44), it is suggested that the binding interactions between SiO₂ and sodium alginate were stronger, increasing the structural stability (solid network) of the gel granule [51,52,61]. This also affected the shape of the granule, as the portion of solid matter (diatomite) interacting with the alginate chains was higher relative to the portion of bound water.

As shown in Figure 1c, the drying process resulted in the evaporation of water from the gel granules composed of diatomite and cross-linked alginate, causing the structure to shrink. During the drying step, the bulk water trapped within the granules evaporated, leading to a closer packing of SiO₂ particles that were initially significantly saturated with water. This was followed by the invasion of air and the gradual emptying of pores [64,65]. The cross-linked alginate network also shrank and collapsed [66] due to the aggregation of chain segments in the junction zones [34,67]. Throughout the shrinkage process, the diatomite particles remained encapsulated in the polymer-like network of the cross-linked alginate, following the distribution pattern of SiO₂ particles within the droplet during the sodium alginate cross-linking process. Consequently, the shape of the heat-treated granules (Figure 5) closely resembled that of the dried granules, accompanied by decreased shrinkage values (D04: 18.45% to D44: 2.53%). After the heat treatment (Figure 1d), the diatomite particles bonded, forming a solid network with inter-particle pores.

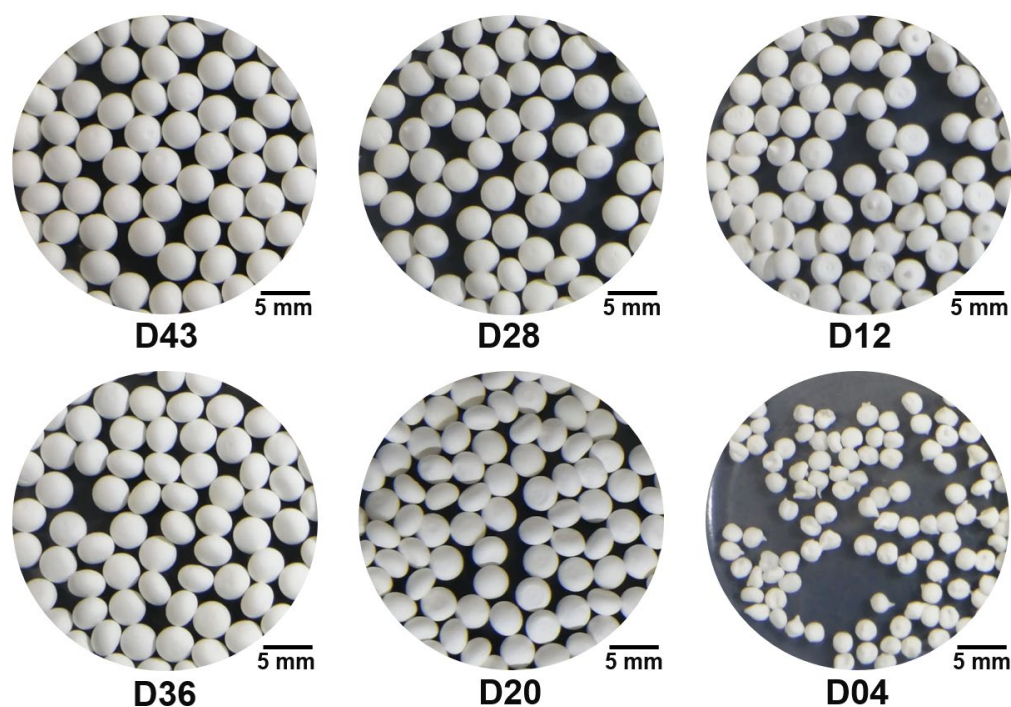


Figure 5. Porous diatomite granules obtained from different dispersion compositions after a heat treatment at 1200 °C for 1 h in air.

Figure 6 presents the sphericity of the diatomite-derived granules as a function of the mass of diatomite in the dispersions (Figure 6a) and the viscosity of the dispersions (Figure 6b). The results indicate that the heat-treated granules prepared with the D04–D16 dispersions (3.85 wt.% to 13.79 wt.%), which displayed viscosities from 273 mPa·s to 429 mPa·s, showed sphericity values between approximately 0.4 and 0.6, exhibiting a tear-like shape (D04) or an ellipsoid shape with a small protrusion (D08–D16). As both the diatomite content (16.67 wt.% to 28.57 wt.%) and the viscosity of the dispersion increased (D20: 468 mPa·s to D40: 1326 mPa·s), the granules presented sphericity values of around 0.7–0.8. The D43 dispersion exhibited the highest sphericity of around 0.9, with a diatomite solid content and viscosity of 30.07 wt.% and 1560 mPa·s, respectively. However,

a slight increase (1.63%) in the solid content (30.56 wt.%) resulted in a significant increase in the viscosity of the D44 dispersion (3160 mPa·s), leading to pear-shaped heat-treated granules with decreased sphericity of approximately 0.5. This suggests that under the fixed processing conditions, there is a diatomite solid content and a viscosity threshold of approximately 30.07 wt.% and 1560 mPa·s, respectively, which can be used to achieve porous diatomite granules with sphericity of around 0.90. Similar trends were observed in CSZ microspheres [22,68] and γ -Al₂O₃ granules [6] under pre-established granulation conditions [6]. The shape of these specimens was improved to achieve a sphericity value close to 1 (sphericity factor close to 0) by increasing the solid matter (raw materials or precursors content) [6,22] or the viscosity of the starting granulation sols [68], until optimized parameters were reached. Beyond this condition, the desired sphericity value could no longer be maintained. Thus, the resultant spherical granule shape is influenced by the optimization of the solid content and the viscosity of the dispersions to stabilize the solid network within the granules and minimize deformations during granulation [40].

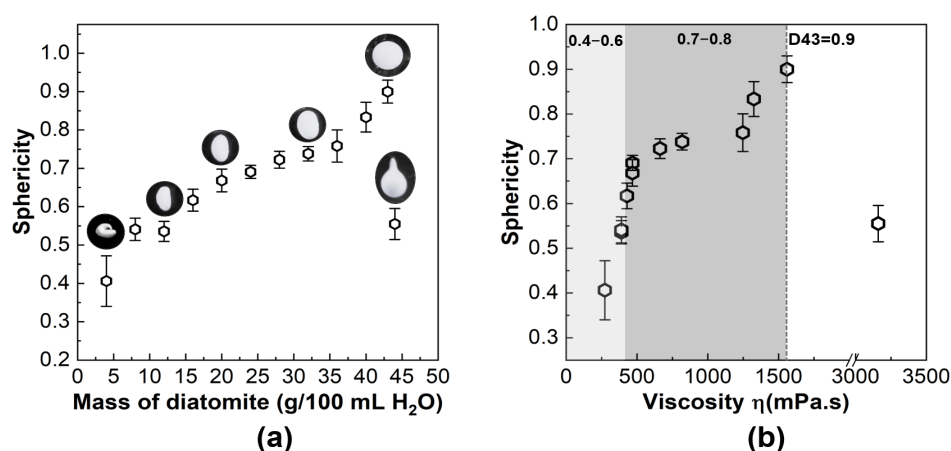


Figure 6. Calculated sphericity of the porous diatomite granules obtained after a heat treatment at 1200 °C for 1 h in air as a function of the (a) mass of diatomite and (b) viscosity of the diatomite/sodium alginate dispersions at a fixed shear rate ($\sim 0.3 \text{ s}^{-1}$, 1 rpm).

Based on the above analysis and considering the tested granulation conditions, the selected diatomite/sodium alginate dispersion composition to ensure millimeter-sized granules (2.60–3.10 mm) with a sphericity of approximately 0.90 is 43 g of diatomite/100 mL H₂O and 1.50 wt.% of sodium alginate. An investigation of alternative granulation parameters, gelling bath conditions, and alginate compositions or additives to optimize the sphericity of the granules processed with higher contents of diatomite (D44: 30.56 wt.%) is beyond the scope of this work. Therefore, the porous diatomite granules for the subsequent experiments were prepared using the fixed D43 dispersion composition and granulation conditions.

3.2. Effect of the Heat-Treatment Temperature on the Properties of the Porous Diatomite Granules

The XRD patterns of the D43 specimens heat-treated between 900 °C to 1200 °C, as compared to the as-received diatomite powders, are presented in Figure 7. The patterns revealed prominent peaks corresponding to cristobalite as the primary crystalline phase, along with minor peaks of quartz. The XRD patterns of the D43-9 and D43-10 specimens closely resembled that of the as-received diatomite, indicating the absence of SiO₂ crystallization during this heat treatment. According to the manufacturer, the as-received diatomite powders is a further purified variety achieved through a flux calcination process carried out between 800 to 1000 °C, using a fluxing agent, commonly Na₂CO₃. The use of Na₂CO₃ aids in lowering the melting point of silica, facilitating the formation of cristobalite even at temperatures as low as 900 °C [69,70]. Based on the XRD patterns of the porous diatomite granules treated at 900 °C and 1000 °C, it is suggested that the primary amorphous

silica to cristobalite phase transformation occurred during the manufacturing process of the as-received diatomite powder. Furthermore, subsequent heat treatment during the processing of the D43-9 and D43-10 specimens did not lead to significant crystallization promotion. However, the D43-11 and D43-12 specimens exhibited increased intensity in the cristobalite peaks with an increase in the heat-treatment temperature. This indicates enhanced crystallization of the amorphous SiO_2 (amorphous SiO_2 content $< 72.5\%$ in the as-received diatomite powders, as shown in Table 1), which is known to be promoted at temperatures higher than $1000\text{ }^\circ\text{C}$ [71]. According to the sintering kinetics of diatomite, the crystallization of cristobalite, along with the densification of particles, is promoted at temperatures exceeding $1000\text{ }^\circ\text{C}$. Therefore, this suggests that a promoted sintering process was observed for the D43-11 specimen, and this process was intensified for the D43-12 specimen [71].

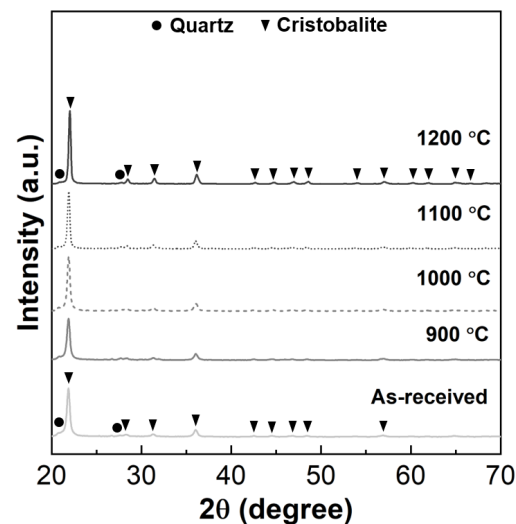


Figure 7. X-ray diffraction patterns of the porous diatomite granules heat-treated between $900\text{ }^\circ\text{C}$ and $1200\text{ }^\circ\text{C}$ as compared to the as-received powder.

As a result, the utilization of purified diatomite powders is proposed to yield an increased fraction of cristobalite, which holds preferential importance in catalytic applications due to its heightened mechanical strength, chemical, and thermal resistance, as well as superior catalytic activity as compared to amorphous SiO_2 [72]. Thus, both the source material and the selected treatment are likely to contribute to the advantageous properties of the resulting porous diatomite granules.

Cross-sectioned microstructures of the D43-0, D43-9, D43-10, D43-11 and D43-12 specimens are presented in Figure 8, while Figure 9 shows typical microstructures of the external surfaces of the specimens. The microstructures of all specimens displayed typical diatomite flake-shaped frustules with characteristic honeycomb-like walls and rod-shaped frustules with pores distributed alongside the edges of the structure [73,74]. For the D43-0 sample, web-like filaments of crosslinked alginate were observed between the diatomite particles, serving as a binding agent that embedded the particles (Figure 9a). It is suggested that, upon heat treatment, CO_2 and H_2O gases are released from the alginate chains, leaving remaining traces of calcium and sodium oxides [75]. With an increase in the temperature, the bonding between the particles was enhanced, which was particularly evidenced in the D43-12 specimen, accompanied by a transition from predominantly small-sized pores to the emergence of large-sized pores, as shown in the regions in Figure 9c.

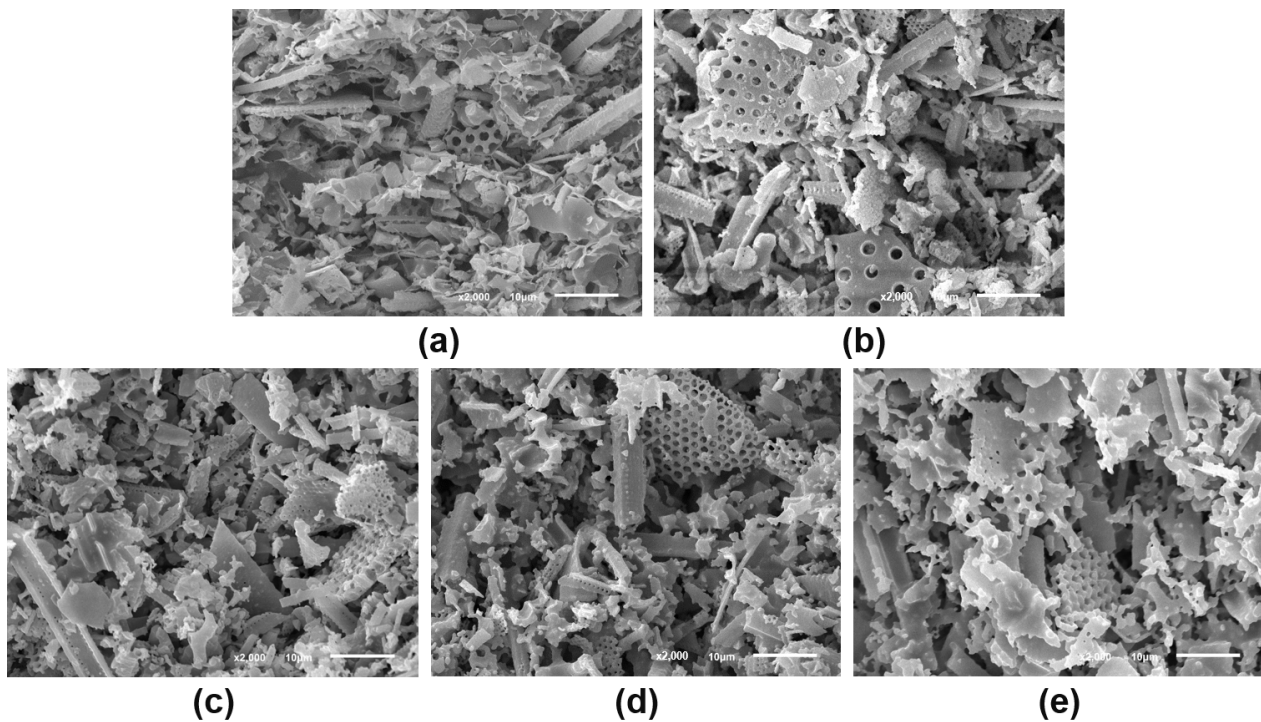


Figure 8. Typical SEM images of cross-sectioned porous diatomite granules: (a) green body, and granules heat-treated at (b) 900 °C, (c) 1000 °C, (d) 1100 °C, and (e) 1200 °C.

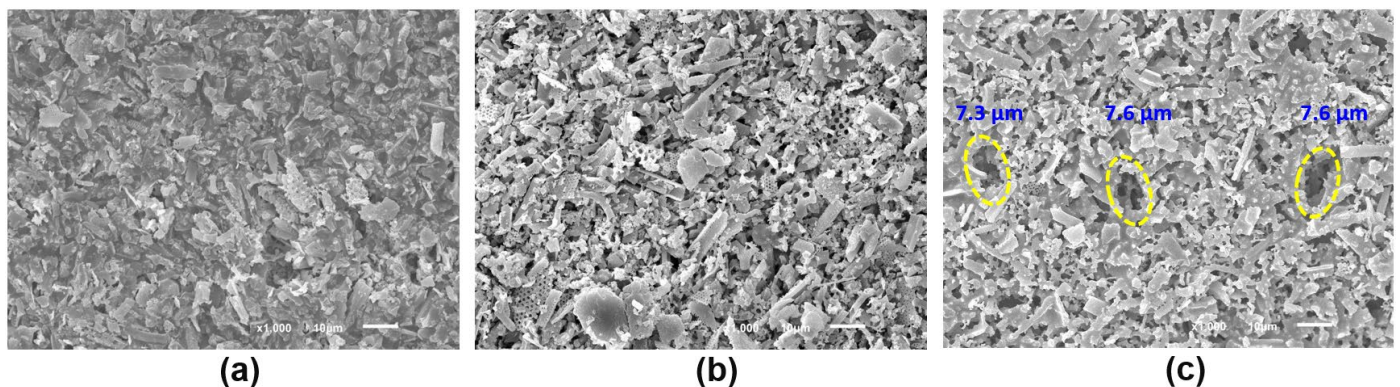


Figure 9. Typical SEM images of the external surface morphologies of porous diatomite granules: (a) green body, and granules heat-treated at (b) 900 °C, and (c) 1200 °C. (Large-sized pores shown in enclosed regions with the corresponding size).

Figure 10 shows the corresponding porosities and bulk densities (Figure 10a), as well as the pore size distributions (Figure 10b) of the D43-9, D43-10, D43-11, and D43-12 specimens. These results indicate gradual partial densification occurring between 900 °C and 1100 °C, as evidenced by a 5.47% increase in the bulk density (accompanied by a 1.88% decrease in the porosity) within this temperature range. Subsequently, with the temperature rising from 1100 °C to 1200 °C, a significant 15.70% increase in the bulk density and a 5.70% decrease in the porosity were observed. This reduction in the porosity was attributed to the facilitated partial densification resulting from the viscous flow of the melt phase formed by amorphous SiO₂ and the impurities present in the as-received diatomite (Al₂O₃, Fe₂O₃, CaO, MgO, Na₂O, and K₂O) [74,76], becoming more pronounced at 1200 °C [71]. Specifically, the oxide impurities within the diatomite particles enabled the formation of low-temperature eutectics, promoting the generation of a melting phase [74,76] and enhancing the coalescence of pores driven by the capillary effect [74,76,77].

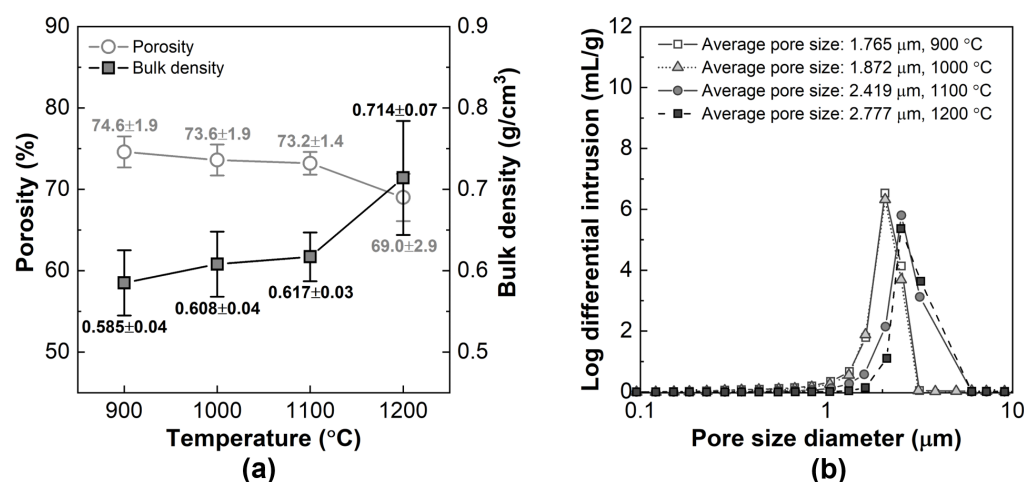


Figure 10. Porosity and bulk density properties (a), and pore size distributions (determined by mercury porosimetry) (b) of porous diatomite granules heat-treated between 900 °C and 1200 °C.

The specimens exhibited unimodal pore size distributions, predominantly corresponding to inter-particle pores [74], with peaks observed at 1.765 μm, 1.872 μm, 2.419 μm, and 2.777 μm for the specimens heat-treated at 900 °C, 1000 °C, 1100 °C, and 1200 °C, respectively. The pore size increased with the temperature, a finding consistent with those in similar reports on γ -Al₂O₃ [3,16,78], TiO₂/ γ -Al₂O₃ [25], and N-doped TiO₂/ γ -Al₂O₃ granules [26] processed through the oil-drop [3,16] and hydrocarbon-ammonia routes [25,26,78]. This phenomenon can be attributed to the enhanced viscous flow of the melt phase, facilitated by the capillarity effect. This effect leads to the penetration or merging of smaller pores, resulting in a decrease in their abundance, and leaving larger pores [76–78]. This phenomenon was observed in the D43-12 specimen, where larger pores were found compared to the predominantly smaller pores observed in the D43-9 sample (Figure 9). Additionally, the logarithmic differential intrusions decreased slightly from 900–1000 °C to 1100–1200 °C, indicating a reduction in the number of open pores due to the improved partial densification between the particles (narrowed inter-particle distance) with an increase in the heat-treatment temperature [74,79]. Moreover, the log differential intrusion area covered pore size diameters ranging from approximately 0.1 μm to 4 μm for the temperature range of 900 °C to 1000 °C, and from around 0.2 μm to 7 μm for the temperature range of 1100 °C to 1200 °C. In this context, the region under the curve correlates with the concentration of pores while the peak point of the curve represents the average pore size [80]. This observation suggests that with an increase in the heat treatment temperature of the porous diatomite granules from 900–1100 °C to 1100–1200 °C, a portion of the log differential intrusion shifts towards larger pore sizes (i.e., an increased presence of larger pores). This shift is illustrated in Figure 9c, depicting the emergence of larger-sized pores (approximately 7 μm).

The N₂ adsorption/desorption isotherms and main properties deduced from the isotherms for the D43-0, D43-9, D43-10, D43-11, and D43-12 specimens are shown in Figure 11 and Table 2, respectively. Overall, the specimens exhibited a minimal amount of N₂ adsorption at low pressures ($p/p_0 < 0.1$), indicating the filling of small micropores (<2 nm) [36,81]. An intermediate region ($0.1 < p/p_0 < 0.9$) was attributed to the adsorption of mesopores (2–50 nm), while a sharp adsorption region at high pressures ($p/p_0 > 0.9$) suggested the presence of abundant macropores (>50 nm) [36,38,81]. Moreover, the samples displayed a hysteresis loop in the high p/p_0 range. According to the IUPAC classification [82], the N₂ adsorption/desorption isotherms of the D43 specimens corresponded to type II isotherms with a H3 hysteresis loops. These characteristics are typically observed in porous solids with hierarchical features and are consistent with diatomite-derived supports [36,38,39,81,83]. Such features are associated with the exis-

tence of meso/macroporosity [39,81] and the presence of slit-shaped pores and non-rigid aggregates of plate-like particles [82].

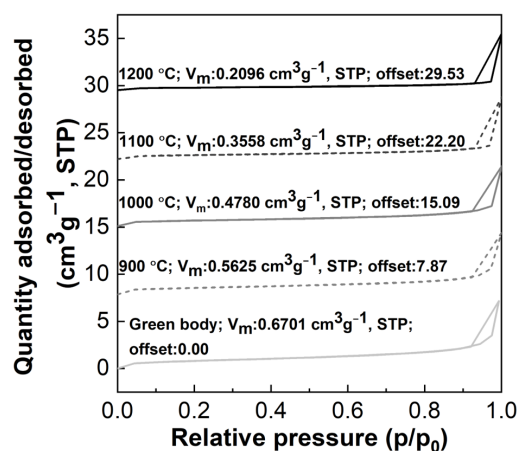


Figure 11. N₂ adsorption/desorption isotherms of porous diatomite granules heat-treated between 900 °C and 1200 °C as compared to the green body. (The adsorbed capacity values and the offsets of the isotherms are included in the label).

The D43 specimens displayed an increase in the average pore size from 14.83 nm to 35.34 nm, accompanied by a decrease in the specific surface area from 2.45 m² g⁻¹ to 0.91 m² g⁻¹ for the D43-9 to D43-12 specimens (Table 2). Additionally, it is suggested that the slight increase in the average pore size of the D43-9 specimen (from 14.70 nm to 14.83 nm) compared to the D43-0 sample can be attributed to the burn-out of the gaseous species from crosslinked alginate chains [11,75]. Figure 11 shows that the adsorption region, with a range of $0.1 < p/p_0 < 0.9$, becomes flatter as the heat-treatment temperature increases, indicating a decrease in the mesoporosity of the specimens [38]. Consequently, the decrease in the specific surface area is mainly governed by a reduction in the mesoporosity due to the filling and merging of smaller pores in the mesopore range, which aligns with the trend observed in the pore size distribution derived from mercury porosimetry (Figure 10b) [3,77,78]. Ultimately, the newly developed porous diatomite granules that were heat-treated between 900 °C to 1200 °C exhibited hierarchical meso/macroporosity, with mesopores in the range of 14.83 nm to 35.34 nm and abundant macroporosity with pore sizes ranging from 1.765 μm to 2.777 μm [39,81].

Table 2. Main properties deduced from the N₂ adsorption/desorption isotherms of the porous diatomite granules heat-treated between 900 °C and 1200 °C as compared with the green body.

Designation	Total Pore Volume (cm ³ g ⁻¹)	Average Pore Diameter (nm)	BET Specific Surface Area (m ² g ⁻¹)
D43-0	0.0107	14.70	2.92
D43-9	0.0091	14.83	2.45
D43-10	0.0088	16.94	2.08
D43-11	0.0089	23.01	1.55
D43-12	0.0081	35.34	0.91

Figure 12, shows the compressive strengths of the D43 specimens heat-treated between 900 °C and 1200 °C as a function of the pore size. The compressive strength outcomes of the newly developed D43 granules were in the corresponding ranges of 0.51 ± 0.09 MPa, 1.17 ± 0.18 MPa, 3.35 ± 0.48 MPa, and 5.17 ± 0.31 MPa for the specimens that were heat-treated at 900 °C, 1000 °C, 1100 °C, and 1200 °C. These results showed that the compressive strengths of the specimens increased with the heat-treatment temperature, which can be attributed to the promoted inter-particle partial densification and decreased porosity [71], particularly evidenced at 1200 °C (porosity of $69.0 \pm 2.9\%$ and bulk density

of $0.714 \pm 0.07 \text{ g/cm}^3$). The D43-9 specimens ($0.51 \pm 0.09 \text{ MPa}$, macropores: $1.765 \mu\text{m}$, mesopores: 14.83 nm) showed a compressive strength value comparable to that of boehmite-derived $\gamma\text{-Al}_2\text{O}_3$ granules (0.95 MPa , pore size: 11.60 nm) obtained under similar processing conditions (sodium alginate gelation) [11]. Furthermore, the D43-12 specimens exhibited a five-fold higher compressive strength ($5.17 \pm 0.31 \text{ MPa}$, macropores: $2.777 \mu\text{m}$, mesopores: 35.34 nm) compared to boehmite-derived $\gamma\text{-Al}_2\text{O}_3$ granules, despite having larger mesopores [11]. Additionally, the newly developed D43-12 granules showed compressive strength comparable to that of porous diatomite granules (5.09 MPa , pore size: $\sim 1.8 \mu\text{m}$) [84] prepared by pan rotation granulation under similar heat-treatment conditions, while also exhibiting hierarchical meso/macroporosity and approximate sphericity of 0.9.

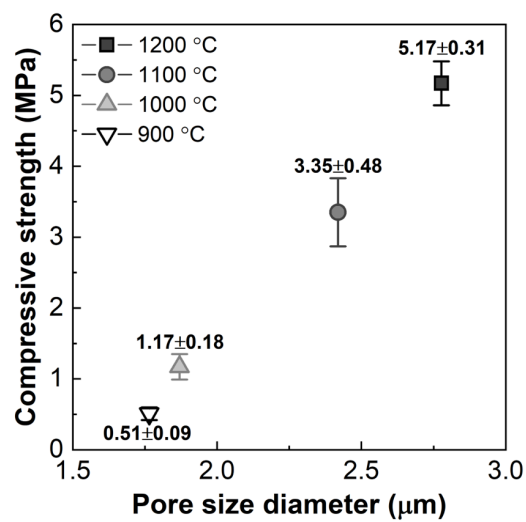


Figure 12. Compressive strength values of porous diatomite granules heat-treated between $900 \text{ }^\circ\text{C}$ and $1200 \text{ }^\circ\text{C}$ as a function of the macropore diameter.

The compressive strength of the granules increased from $0.51 \pm 0.09 \text{ MPa}$ to $5.17 \pm 0.31 \text{ MPa}$ as the heat-treatment temperatures increased from $900 \text{ }^\circ\text{C}$ to $1200 \text{ }^\circ\text{C}$, while the specific surface area decreased from $2.45 \text{ m}^2 \text{ g}^{-1}$ to $0.91 \text{ m}^2 \text{ g}^{-1}$. This indicates a trade-off relationship between these two properties. Nevertheless, the specimens exhibited a hierarchical meso/macropore structure irrespective of the heat-treatment condition. Despite having a lower specific surface area, the D43-9 and D43-12 specimens showed mesopore sizes comparable to those of boehmite-derived $\gamma\text{-Al}_2\text{O}_3$ granules (S_{BET} : $244.0 \text{ m}^2 \text{ g}^{-1}$, 14.83 nm) [11] and oil-molding derived $\gamma\text{-Al}_2\text{O}_3$ granules (S_{BET} : $7.0 \text{ m}^2 \text{ g}^{-1}$, 39.92 nm) [16], which were obtained through similar heat treatments and are applicable as catalytic supports. Furthermore, the newly developed D43-9 granules ($2.45 \text{ m}^2 \text{ g}^{-1}$, mesopore size: 14.83 nm) exhibited a specific surface area comparable to that of the CaO/carbon catalyst beads used in CO_2 reduction ($2.03 \text{ m}^2 \text{ g}^{-1}$, 1.8 nm , N_2 calcination, $500 \text{ }^\circ\text{C}$) [85]. Additionally, the D43-9 and D43-12 specimens displayed mesoporosity and macroporosity ranges similar to those of non-consolidated diatomite supports (mesopore size: $\sim 30 \text{ nm}$ [38], macropore size: $\sim 0.1\text{--}3.2 \mu\text{m}$ [81]) of the type used for the adsorption of organic pollutants [36,38] and heavy metals [36]. The macroporosity in these systems is considered highly beneficial for adsorption applications, as it enhances the efficiency of the mass transport and diffusion process [38].

In summary, our newly developed D43-9 specimens showed compressive strength comparable to that of sodium alginate gelation-derived $\gamma\text{-Al}_2\text{O}_3$ granules [11] along with comparable mesoporosity. Similarly, the D43-12 specimens displayed mesoporosity analogous to oil-molding derived $\gamma\text{-Al}_2\text{O}_3$ granules [16], both of which find applications in fluidized bed reactors. Furthermore, the D43-12 granules demonstrated compressive strength comparable to that of porous diatomite granules processed through a complex pan rotation process, which are also applicable to fluidized bed reactors [84], and the D43-12

granules exhibited a consolidated form while presenting meso/macroporosity similar to that of the non-consolidated diatomite supports used for adsorption applications [36,38,81].

Accordingly, the proposed manufacturing method successfully facilitated the development of hierarchically porous diatomite granules with high sphericity and compressive strengths comparable to those of similar porous materials reported in the literature. The presence of hierarchical porosity in millimeter-sized spherical materials is highly desirable for their application as a support material for catalytic and adsorption purposes. This is due to factors including (1) the functionality associated with the mesopores, (2) the good mechanical and chemical stability attributed to the macroporosity [5,11], and (3) the advantageous fluid transport facilitated by both the hierarchical nature and the material's spherical shape [5,6]. Consequently, the newly obtained porous diatomite granules possess a combination of features that make them potential porous support materials for catalytic and adsorption applications, similar to those discussed in the literature.

4. Conclusions

In this study, porous diatomite granules were prepared by the dropwise granulation of diatomite/sodium alginate dispersions involving sodium alginate cross-linking and subsequent heat treatment ranging from 900 °C to 1200 °C. The dispersions were formulated with solid loadings of diatomite ranging from 3.8 to 30.5 wt.% (4 to 44 g/100 mL H₂O) while maintaining a fixed sodium alginate content. The assessment of the properties throughout the manufacturing process yielded the following key findings:

The optimization of the solid content and viscosity of the dispersions to 30.07 wt.% and 1560 mPa.s (~0.3 s⁻¹ shear rate), respectively, ensured a uniform solid network within the granules, which minimized deformations under fixed granulation conditions and resulted in granules with a maximum sphericity of ~0.90.

The porous diatomite granules exhibited a decrease in the total porosity from 74.6 ± 1.9% to 69.0 ± 2.9%, an outcome attributed to the enhanced partial densification as the heat-treatment temperature was increased from 900 °C to 1200 °C. Additionally, these granules displayed a hierarchical structure consisting of macropores ranging from 1.769 μm to 2.777 μm and mesopores ranging from 14.83 nm to 35.34 nm. The pore sizes increased due to the facilitated filling and merging of smaller pores with an increase in the temperature.

A trade-off relationship was evidenced between the compressive strengths and the specific surface areas of the porous diatomite granules as a function of the temperature. The compressive strengths increased from 0.51 ± 0.09 MPa to 5.17 ± 0.31 MPa while the specific surface areas simultaneously decreased from 2.45 m²/g to 0.49 m²/g. However, it is noteworthy that the diatomite granules consistently displayed hierarchical meso/microporosity, independent of the heat-treatment conditions.

In summary, the newly developed millimeter-sized porous diatomite granules exhibited high sphericity, hierarchical porosity, and acceptable compressive strengths comparable to those of porous γ-Al₂O₃ granules derived from sodium alginate gelation and porous diatomite granules, obtained through pan rotation granulation. These characteristics highlight the potential applicability of these granules as support materials for catalytic and adsorption purposes.

Supplementary Materials: The following supporting information can be downloaded at: <https://www.mdpi.com/article/10.3390/app13169474/s1>, Figure S1: Scheme illustrating the ball-milling conditions and the processed diatomite slurries used to prepare the diatomite/sodium alginate dispersions and, subsequently, the porous diatomite granules; Figure S2: Representative porous diatomite granules (D08-D24) obtained after each step in the processing route: (a) aging (CaCl₂ bath) and cleaning (DI water), (b) drying (80 °C, overnight), and (c) a heat treatment at 1200 °C for 1 h in air; Figure S3: Representative porous diatomite granules (D28-D40) obtained after each step in the processing route: (a) aging (CaCl₂ bath) and cleaning (DI water), (b) drying (80 °C, overnight), and (c) a heat treatment at 1200 °C for 1 h in air.

Author Contributions: J.-H.H. and I.-H.S. conceived and designed the experiments; E.-J.O. and M.D.S.L. performed the experiments; J.L., H.-J.L. and J.-H.H. analyzed the data; I.-H.S. contributed reagents/materials/analysis tools; M.D.S.L. wrote the paper. All authors have read and agreed to the published version of the manuscript.

Funding: This research was funded by the Fundamental Research Program of the Korean Institute of Materials Science (KIMS), through Grant No. PNK8810, and by the Technology Innovation Program (20003782) of the Ministry of Trade, Industry and Energy.

Institutional Review Board Statement: Not applicable.

Informed Consent Statement: Not applicable.

Data Availability Statement: The data presented in this study are available in "Effects of Processing Conditions on the Properties of Porous Diatomite Granules Prepared by Sodium Alginate Gelation".

Acknowledgments: This research was funded by the Fundamental Research Program of the Korean Institute of Materials Science (KIMS), through Grant No. PNK8810, and by the Technology Innovation Program (20003782) of the Ministry of Trade, Industry and Energy. And the authors are sincerely grateful to Seung Hwa Jung and Jun Young Shin (R&D Center, Cenotec Co., Ltd., 1256-40, Hama-Dearo, Gaya-Eup, Haman-Gun, Gyeongsangnam-do, 52035, Republic of Korea) for their contribution with reagents, materials, and analysis tools.

Conflicts of Interest: The authors declare no conflict of interest.

References

- Ohji, T.; Fukushima, M. Macro-porous ceramics: Processing and properties. *Int. Mater. Rev.* **2012**, *57*, 115–131. [\[CrossRef\]](#)
- Chen, Y.; Wang, N.N.; Ola, O.; Xia, Y.D.; Zhu, Y.Q. Porous ceramics: Light in weight but heavy in energy and environment technologies. *Mat. Sci. Eng. R* **2021**, *143*, 100589. [\[CrossRef\]](#)
- Abdollahi, M.; Atashi, H.; Tabrizi, F.F. Parametric investigation of γ -alumina granule preparation via the oil-drop route. *Adv. Powder Technol.* **2017**, *28*, 1356–1371. [\[CrossRef\]](#)
- Yang, Z.H.; Lin, Y.S. Sol-gel synthesis of silicalite/ γ -alumina granules. *Ind. Eng. Chem. Res.* **2000**, *39*, 4944–4948. [\[CrossRef\]](#)
- Colombo, P.; Vakifahmetoglu, C.; Costacurta, S. Fabrication of ceramic components with hierarchical porosity. *J. Mater. Sci.* **2010**, *45*, 5425–5455. [\[CrossRef\]](#)
- Islam, A.; Taufiq-Yap, Y.H.; Chu, C.M.; Chan, E.S.; Ravindra, P. Synthesis and characterization of millimetric gamma alumina spherical particles by oil drop granulation method. *J. Porous Mat.* **2012**, *19*, 807–817. [\[CrossRef\]](#)
- Teo, S.H.; Yap, D.K.Y.; Mansir, N.; Islam, A.; Taufiq-Yap, Y.H. Facile Recoverable and Reusable Macroscopic Alumina Supported Ni-based Catalyst for Efficient Hydrogen Production. *Sci. Rep.* **2019**, *9*, 16358. [\[CrossRef\]](#)
- Martín, E.; Alarcón, A.; Xuriguera, E.; Guilera, J. Shaping of Porous CeO₂ Powders into Highly Active Catalyst Carriers. *ACS Appl. Eng. Mater.* **2023**, *1*, 1106–1115. [\[CrossRef\]](#)
- Li, J.; Wu, M.J.; Du, H.C.; Wang, B.C.; Li, Y.L.; Huan, W.W. Highly effective catalytic reduction of nitrobenzene compounds with gold nanoparticle-immobilized hydroxyapatite nanowire-sintered porous ceramic beads. *New J. Chem.* **2021**, *45*, 4601–4610. [\[CrossRef\]](#)
- Patcas, F.C.; Garrido, G.I.; Kraushaar-Czarnetzki, B. CO oxidation over structured carriers: A comparison of ceramic foams, honeycombs and beads. *Chem. Eng. Sci.* **2007**, *62*, 3984–3990. [\[CrossRef\]](#)
- Islam, A.; Taufiq-Yap, Y.H.; Ravindra, P.; Moniruzzaman, M.; Chan, E.S. Development of a procedure for spherical alginate-boehmite particle preparation. *Adv. Powder Technol.* **2013**, *24*, 1119–1125. [\[CrossRef\]](#)
- Islam, A.; Taufiq-Yap, Y.H.; Ravindra, P.; Teo, S.H.; Sivasangar, S.; Chan, E.S. Biodiesel synthesis over millimetric γ -Al₂O₃/KI catalyst. *Energy* **2015**, *89*, 965–973. [\[CrossRef\]](#)
- Ismagilov, Z.R.; Shkrabina, R.A.; Koryabkina, N.A. New technology for production of spherical alumina supports for fluidized bed combustion. *Catal. Today* **1999**, *47*, 51–71. [\[CrossRef\]](#)
- Ismagilov, Z.R.; Shkrabina, R.A.; Koryabkina, N.A. Hydrocarbon-ammonia moulding—a new technology for production of combustion catalysts. *Korean J. Chem. Eng.* **1997**, *14*, 153–161. [\[CrossRef\]](#)
- Wang, G.G.; Ma, J.T.; Gao, Y.; Zhao, X.Y.; Hao, S.C.; Deng, C.S.; Liu, B. A comparative study of small-size ceria-zirconia microspheres fabricated by external and internal gelation. *J. Sol. Gel Sci. Technol.* **2016**, *78*, 673–681. [\[CrossRef\]](#)
- Beiknejad, D. Synthesis optimization, structural evolution and optical properties of hierarchical nanoporous alumina microspheres prepared by continuous soft chemistry method. *J. Porous Mat.* **2013**, *20*, 1075–1086. [\[CrossRef\]](#)
- Buelna, G.; Lin, Y.S. Sol-gel-derived mesoporous γ -alumina granules. *Microporous Mesoporous Mater.* **1999**, *30*, 359–369. [\[CrossRef\]](#)
- Liu, P.C.; Feng, J.T.; Zhang, X.M.; Lin, Y.J.; Evans, D.G.; Li, D.Q. Preparation of high purity spherical γ -alumina using a reduction-magnetic separation process. *J. Phys. Chem. Solids* **2008**, *69*, 799–804. [\[CrossRef\]](#)
- Gangar, B.V.; Nagarajan, K.; Krishnan, R.V.; Pandit, A.B. Preparation of Alumina and Alumina-Ceria Microspheres using an Internal Gelation Process and their Characterization. *Trans. Indian Ceram. Soc.* **2012**, *71*, 101–109. [\[CrossRef\]](#)

20. Couland, M.; Fourcaudot, S.; Abril, R.J.; Fernandez-Carretero, A.; Somers, J. Novel Production Route of Yttria-Stabilized Zirconia Fuel Kernels and Pellets for Nuclear Fuel Applications. *J. Am. Ceram. Soc.* **2012**, *95*, 133–137. [[CrossRef](#)]
21. Ding, X.Q.; Ma, J.T.; Zhou, X.W.; Zhao, X.Y.; Hao, S.C.; Deng, C.S.; Li, G.X. Fabrication of CeO₂-Nd₂O₃ microspheres by internal gelation process using M(OH)_m and [MCit·xH₂O] (M=Ce³⁺, Ce⁴⁺, and Nd³⁺) as precursors. *J. Sol. Gel Sci. Technol.* **2019**, *92*, 66–74. [[CrossRef](#)]
22. Wang, G.G.; Ma, J.T.; Gao, Y.; Zhao, X.Y.; Hao, S.C.; Deng, C.S.; Liu, B. Preparation of ceria-stabilized zirconia microspheres by external gelation: Size control. *J. Sol. Gel Sci. Technol.* **2016**, *78*, 514–522. [[CrossRef](#)]
23. Jang, C.R.; Han, K.B.; Voicu, V.; Matei, V.; Ciuparu, D. Impregnation of Catalytic Active Components in an Ammonia Solution During Granulation of Aluminium Hydroxide Gel by Sol-Gel Method in Hydrocarbon-Ammonia Moulding Column. *Rev. Chim.* **2012**, *63*, 1301–1305.
24. Chen, J.C.; Tang, C.T. Preparation and application of granular ZnO/Al₂O₃ catalyst for the removal of hazardous trichloroethylene. *J. Hazard Mater.* **2007**, *142*, 88–96. [[CrossRef](#)]
25. Choi, J.S.; Ban, J.Y.; Choung, S.J.; Kim, J.S.; Abimanyu, H.; Yoo, K.S. Sol-gel synthesis, characterization and photocatalytic activity of mesoporous TiO₂/γ-Al₂O₃ granules. *J. Sol. Gel Sci. Technol.* **2007**, *44*, 21–28. [[CrossRef](#)]
26. Huang, D.G.; Xie, W.F.; Tu, Z.B.; Zhang, F.; Quan, S.Q.; Liu, L. N-TiO₂/gamma-Al₂O₃ Granules: Preparation, Characterization and Photocatalytic Activity for the Degradation of 2,4-Dichlorophenol. *J. Nanosci. Nanotechnol.* **2013**, *13*, 260–269. [[CrossRef](#)]
27. Liang, S.S.; Wang, C.L.; Li, Y.J.; Xu, M.Z.; Jia, H. Microfluidic fabrication of ZrO₂ microspheres using improved external gelation aided by polyacrylamide networks. *Ceram. Int.* **2021**, *47*, 21576–21581. [[CrossRef](#)]
28. Backov, R. Combining soft matter and soft chemistry: Integrative chemistry towards designing novel and complex multiscale architectures. *Soft Matter* **2006**, *2*, 452–464. [[CrossRef](#)]
29. Prouzet, E.; Khani, Z.; Bertrand, M.; Tokumoto, M.; Guyot-Ferreol, V.; Tranchant, J.F. An example of integrative chemistry: Combined gelation of boehmite and sodium alginate for the formation of porous beads. *Microporous Mesoporous Mater.* **2006**, *96*, 369–375. [[CrossRef](#)]
30. Danks, A.E.; Hall, S.R.; Schnepf, Z. The evolution of ‘sol-gel’ chemistry as a technique for materials synthesis. *Mater. Horiz.* **2016**, *3*, 91–112. [[CrossRef](#)]
31. Cao, L.Q.; Lu, W.; Mata, A.; Nishinari, K.; Fang, Y.P. Egg-box model-based gelation of alginate and pectin: A review. *Carbohydr. Polym.* **2020**, *242*, 116389. [[CrossRef](#)] [[PubMed](#)]
32. Sergeeva, A.; Vikulina, A.S.; Volodkin, D. Porous Alginate Scaffolds Assembled Using Vaterite CaCO₃ Crystals. *Micromachines* **2019**, *10*, 357. [[CrossRef](#)] [[PubMed](#)]
33. Roger, S.; Talbot, D.; Bee, A. Preparation and effect of Ca²⁺ on water solubility, particle release and swelling properties of magnetic alginate films. *J. Magn. Magn. Mater.* **2006**, *305*, 221–227. [[CrossRef](#)]
34. Li, L.B.; Fang, Y.P.; Vreeker, R.; Appelqvist, I.; Mendes, E. Reexamining the egg-box model in calcium-alginate gels with X-ray diffraction. *Biomacromolecules* **2007**, *8*, 464–468. [[CrossRef](#)]
35. Harper, B.A.; Barbut, S.; Lim, L.T.; Marcone, M.F. Effect of Various Gelling Cations on the Physical Properties of “Wet” Alginate Films. *J. Food Sci.* **2014**, *79*, E562–E567. [[CrossRef](#)]
36. Liu, P.; He, H.P.; Wei, G.L.; Liu, D.; Liang, X.L.; Chen, T.H.; Zhu, J.X.; Zhu, R.L. An efficient catalyst of manganese supported on diatomite for toluene oxidation: Manganese species, catalytic performance, and structure activity relationship. *Microporous Mesoporous Mater.* **2017**, *239*, 101–110. [[CrossRef](#)]
37. Lee, S.; Lee, C.Y.; Ha, J.H.; Lee, J.; Song, I.H.; Kwon, S.H. Effect of Processing Conditions on the Properties of Reticulated Porous Diatomite-Kaolin Composites. *Appl. Sci.* **2020**, *10*, 7297. [[CrossRef](#)]
38. Yu, W.B.; Deng, L.L.; Yuan, P.; Liu, D.; Yuan, W.W.; Liu, P.; He, H.P.; Li, Z.H.; Chen, F.R. Surface silylation of natural mesoporous/macroporous diatomite for adsorption of benzene. *J. Colloid Interface Sci.* **2015**, *448*, 545–552. [[CrossRef](#)]
39. Yuan, P.; Liu, D.; Fan, M.D.; Yang, D.; Zhu, R.L.; Ge, F.; Zhu, J.X.; He, H.P. Removal of hexavalent chromium [Cr(VI)] from aqueous solutions by the diatomite-supported/unsupported magnetite nanoparticles. *J. Hazard Mater.* **2010**, *173*, 614–621. [[CrossRef](#)]
40. Davarci, F.; Turan, D.; Ozcelik, B.; Poncelet, D. The influence of solution viscosities and surface tension on calcium-alginate microbead formation using dripping technique. *Food Hydrocolloid* **2017**, *62*, 119–127. [[CrossRef](#)]
41. Chan, E.S.; Lee, B.B.; Ravindra, P.; Poncelet, D. Prediction models for shape and size of ca-alginate macrobeads produced through extrusion-dripping method. *J. Colloid Interface Sci.* **2009**, *338*, 63–72. [[CrossRef](#)]
42. Chen, C.H.; Gu, J.Y.; Peng, Z.S.; Dai, X.Y.; Liu, Q.B.; Zhu, G.Q. Discrete element modeling of particles sphericity effect on sand direct shear performance. *Sci. Rep.* **2022**, *12*, 5490. [[CrossRef](#)]
43. ISO 18754:2013; Fine Ceramics (Advanced Ceramics, Advanced Technical Ceramics)—Determination of Density and Apparent Porosity. International Organization for Standardization (ISO): Geneva, Switzerland, 2013; pp. 1–7.
44. Lucio, M.D.S.; Kultayeva, S.; Kim, Y.W.; Song, I.H. Effects of SiC whisker addition on mechanical, thermal, and permeability properties of porous silica-bonded SiC ceramics. *Int. J. Appl. Ceram. Technol.* **2022**, *19*, 1439–1452. [[CrossRef](#)]
45. Kim, J.M.; Kim, H.N.; Park, Y.J.; Ko, J.W.; Lee, J.W.; Kim, H.D. Fabrication of transparent MgAl₂O₄ spinel through homogenous green compaction by microfluidization and slip casting. *Ceram. Int.* **2015**, *41*, 13354–13360. [[CrossRef](#)]
46. Olhero, S.M.; Ferreira, J.M.F. Influence of particle size distribution on rheology and particle packing of silica-based suspensions. *Powder Technol.* **2004**, *139*, 69–75. [[CrossRef](#)]

47. Lee, C.Y.; Lee, S.; Ha, J.H.; Lee, J.; Song, I.H.; Moon, K.S. Effect of the Zirconia Particle Size on the Compressive Strength of Reticulated Porous Zirconia-Toughened Alumina. *Appl. Sci.* **2022**, *12*, 2316. [[CrossRef](#)]
48. Lee, C.Y.; Lee, S.; Ha, J.H.; Lee, J.; Song, I.H.; Moon, K.S. Effect of the Sintering Temperature on the Compressive Strengths of Reticulated Porous Zirconia. *Appl. Sci.* **2021**, *11*, 5672. [[CrossRef](#)]
49. Chen, S.; Wang, C.S.; Zheng, W.; Wu, J.M.; Yan, C.Z.; Shi, Y.S. Effects of particle size distribution and sintering temperature on properties of alumina mold material prepared by stereolithography. *Ceram. Int.* **2022**, *48*, 6069–6077. [[CrossRef](#)]
50. Qian, C.C.; Hu, K.H.; Wang, H.Y.; Nie, L.; Feng, Q.; Lu, Z.G.; Li, P.J.; Lu, K. The effect of particle size distribution on the microstructure and properties of Al₂O₃ ceramics formed by stereolithography. *Ceram. Int.* **2022**, *48*, 21600–21609. [[CrossRef](#)]
51. Wang, S.; Huang, X.; Elimelech, M. Complexation between dissolved silica and alginate molecules: Implications for reverse osmosis membrane fouling. *J. Membr. Sci.* **2020**, *605*, 118109. [[CrossRef](#)]
52. Han, X.H.; Liang, J.C.; Fukuda, S.; Zhu, L.J.; Wang, S.R. Sodium alginate-silica composite aerogels from rice husk ash for efficient absorption of organic pollutants. *Biomass Bioenergy* **2022**, *159*, 106424. [[CrossRef](#)]
53. Hou, L.; Wu, P.Y. Exploring the hydrogen-bond structures in sodium alginate through two-dimensional correlation infrared spectroscopy. *Carbohydr. Polym.* **2019**, *205*, 420–426. [[CrossRef](#)]
54. Lowe, B.M.; Skylaris, C.K.; Green, N.G. Acid-base dissociation mechanisms and energetics at the silica-water interface: An activationless process. *J. Colloid Interface Sci.* **2015**, *451*, 231–244. [[CrossRef](#)] [[PubMed](#)]
55. Shinde, U.A.; Nagarsenker, M.S. Characterization of Gelatin-Sodium Alginate Complex Coacervation System. *Indian J. Pharm. Sci.* **2009**, *71*, 313–317. [[CrossRef](#)]
56. Hutin, A.; Lima, N.; Lopez, F.; Carvalho, M. Stability of Silica Nanofluids at High Salinity and High Temperature. *Powders* **2023**, *2*, 1–20. [[CrossRef](#)]
57. Mei, S.; Yang, J.; Ferreira, J.M.F. Effect of dispersant concentration on slip casting of cordierite-based glass ceramics. *J. Colloid Interface Sci.* **2001**, *241*, 417–421. [[CrossRef](#)]
58. Yang, H.B.; Kang, W.L.; Wu, H.R.; Yu, Y.; Zhu, Z.; Wang, P.X.; Zhang, X.F.; Sarsenbekuly, B. Stability, rheological property and oil-displacement mechanism of a dispersed low-elastic microsphere system for enhanced oil recovery. *RSC Adv.* **2017**, *7*, 8118–8130. [[CrossRef](#)]
59. Wagner, N.J.; Brady, J.F. Shear thickening in colloidal dispersions. *Phys. Today* **2009**, *62*, 27–32. [[CrossRef](#)]
60. Ribeiro, M.P.; da Silveira, P.H.P.M.; Braga, F.D.; Monteiro, S.N. Fabric Impregnation with Shear Thickening Fluid for Ballistic Armor Polymer Composites: An Updated Overview. *Polymers* **2022**, *14*, 4357. [[CrossRef](#)]
61. Shi, J.F.; Zhang, H.; Yu, Y.; Zou, X.Q.; Zhou, W.D.; Guo, J.; Ye, Y.M.; Zhao, Y.H. Adsorption Properties of Calcium Alginate-Silica Dioxide Hybrid Adsorbent to Methylene Blue. *J. Inorg. Organomet. Polym. Mater.* **2020**, *30*, 2114–2125. [[CrossRef](#)]
62. Voo, W.P.; Ooi, C.W.; Islam, A.; Tey, B.T.; Chan, E.S. Calcium alginate hydrogel beads with high stiffness and extended dissolution behaviour. *Eur. Polym. J.* **2016**, *75*, 343–353. [[CrossRef](#)]
63. Murer, M.; Formica, G.; Milicchio, F.; Morganti, S.; Auricchio, F. A coupled multiphase Lagrangian-Eulerian fluid-dynamics framework for numerical simulation of Laser Metal Deposition process. *Int. J. Adv. Manuf. Technol.* **2022**, *120*, 3269–3286. [[CrossRef](#)]
64. Peixinho, J.; Lefevre, G.; Coudert, F.X.; Hurisse, O. Water evaporation in silica colloidal deposits. *J. Colloid Interface Sci.* **2013**, *408*, 206–211. [[CrossRef](#)] [[PubMed](#)]
65. van der Kooij, H.M.; van de Kerkhof, G.T.; Sprakel, J. A mechanistic view of drying suspension droplets. *Soft Matter* **2016**, *12*, 2858–2867. [[CrossRef](#)] [[PubMed](#)]
66. Labowska, M.B.; Skrodzka, M.; Sicinska, H.; Michalak, I.; Detyna, J. Influence of Cross-Linking Conditions on Drying Kinetics of Alginate Hydrogel. *Gels* **2023**, *9*, 63. [[CrossRef](#)]
67. Vreeker, R.; Li, L.B.; Fang, Y.P.; Appelqvist, I.; Mendes, E. Drying and Rehydration of Calcium Alginate Gels. *Food Biophys.* **2008**, *3*, 361–369. [[CrossRef](#)]
68. Wang, G.G.; Ma, J.T.; Gao, Y.; Zhao, X.Y.; Hao, S.C.; Deng, C.S. Precisely Controlling Preparation of Ceria-Stabilized Zirconia Microspheres of similar to ~ 100 μm by External Gelation. *Int. J. Appl. Ceram. Technol.* **2016**, *13*, 831–837. [[CrossRef](#)]
69. Kupkova, J.; Valaskova, M.; Studentova, S. Influence of acid-treated talc and Na₂CO₃ flux on mineralogical phase composition and porosity in steatite ceramics. *Int. J. Appl. Ceram. Technol.* **2017**, *14*, 803–809. [[CrossRef](#)]
70. Dapiaggi, M.; Pagliari, L.; Pavese, A.; Sciascia, L.; Merli, M.; Francescon, F. The formation of silica high temperature polymorphs from quartz: Influence of grain size and mineralising agents. *J. Eur. Ceram. Soc.* **2015**, *35*, 4547–4555. [[CrossRef](#)]
71. Zhang, X.B.; Liu, X.Q.; Meng, G.Y. Sintering kinetics of porous ceramics from natural diatomite. *J. Am. Ceram. Soc.* **2005**, *88*, 1826–1830. [[CrossRef](#)]
72. Jiang, X.M.; Bao, L.H.; Cheng, Y.S.; Dunphy, D.R.; Li, X.D.; Brinker, C.J. Aerosol-assisted synthesis of monodisperse single-crystalline alpha-cristobalite nanospheres. *Chem. Commun.* **2012**, *48*, 1293–1295. [[CrossRef](#)] [[PubMed](#)]
73. Zhang, D.Y.; Wang, Y.; Cai, J.; Pan, J.F.; Jiang, X.G.; Jiang, Y.G. Bio-manufacturing technology based on diatom micro- and nanostructure. *Chin. Sci. Bull.* **2012**, *57*, 3836–3849. [[CrossRef](#)]
74. Saponjic, A.; Stankovic, M.; Majstorovic, J.; Matovic, B.; Ilic, S.; Egelja, A.; Kokunesoski, M. Porous ceramic monoliths based on diatomite. *Ceram. Int.* **2015**, *41*, 9745–9752. [[CrossRef](#)]
75. Araujo, P.D.; Belini, G.B.; Mambriani, G.P.; Yamaji, F.M.; Waldman, W.R. Thermal degradation of calcium and sodium alginate: A greener synthesis towards calcium oxide micro/nanoparticles. *Int. J. Biol. Macromol.* **2019**, *140*, 749–760. [[CrossRef](#)]

76. Akhtar, F.; Rehman, Y.; Bergstrom, L. A study of the sintering of diatomaceous earth to produce porous ceramic monoliths with bimodal porosity and high strength. *Powder Technol.* **2010**, *201*, 253–257. [[CrossRef](#)]
77. Whittemore, O.J.; Sipe, J.J. Pore growth during the initial stages of sintering ceramics. *Powder Technol.* **1974**, *9*, 159–164. [[CrossRef](#)]
78. Shabani, S.; Mirkazemi, S.M.; Rezaie, H.; Vahidshad, Y.; Trasatti, S. A comparative study on the thermal stability, textural, and structural properties of mesostructured γ -Al₂O₃ granules in the presence of La, Sn, and B additives. *Ceram. Int.* **2022**, *48*, 6638–6648. [[CrossRef](#)]
79. Lee, S.; Ha, J.H.; Lee, J.; Song, I.H. Enhanced mechanical strength of talc-containing porous kaolin prepared by a replica method. *J. Korean Ceram. Soc.* **2021**, *58*, 123–133. [[CrossRef](#)]
80. Shaikh, F.U.A.; Supit, S.W.M. Compressive strength and durability of high-volume fly ash concrete reinforced with calcium carbonate nanoparticles. In *Fillers and Reinforcements for Advanced Nanocomposites*; Dong, Y., Umer, R., Lau, A.K.-T., Eds.; Woodhead Publishing: Sawston, UK, 2015; pp. 275–307.
81. Yuan, W.W.; Yuan, P.; Liu, D.; Deng, L.L.; Zhou, J.M.; Yu, W.B.; Chen, F.R. A hierarchically porous diatomite/silicalite-1 composite for benzene adsorption/desorption fabricated via a facile pre-modification in situ synthesis route. *Chem. Eng. J.* **2016**, *294*, 333–342. [[CrossRef](#)]
82. Thommes, M.; Kaneko, K.; Neimark, A.V.; Olivier, J.P.; Rodriguez-Reinoso, F.; Rouquerol, J.; Sing, K.S.W. Physisorption of gases, with special reference to the evaluation of surface area and pore size distribution (IUPAC Technical Report). *Pure Appl. Chem.* **2015**, *87*, 1051–1069. [[CrossRef](#)]
83. Kumar, K.V.; Gadipelli, S.; Wood, B.; Ramisetty, K.A.; Stewart, A.A.; Howard, C.A.; Brett, D.J.L.; Rodriguez-Reinoso, F. Characterization of the adsorption site energies and heterogeneous surfaces of porous materials. *J. Mater. Chem. A* **2019**, *7*, 10104–10137. [[CrossRef](#)]
84. Liu, Y.J.; Scharf, D.; Graule, T.; Clemens, F.J. Granulation processing parameters on the mechanical properties of diatomite-based porous granulates. *Powder Technol.* **2014**, *263*, 159–167. [[CrossRef](#)]
85. Prasanna, D.V.; Ramanan, M.V. Experimental analysis of CO₂ reduction using low surface area carbon beads (CB) and Ca/CB catalyst by thermocatalytic gasification for fuel gas production. *Biomass Convers. Biorefinery* **2023**, *13*, 7319–7331. [[CrossRef](#)]

Disclaimer/Publisher's Note: The statements, opinions and data contained in all publications are solely those of the individual author(s) and contributor(s) and not of MDPI and/or the editor(s). MDPI and/or the editor(s) disclaim responsibility for any injury to people or property resulting from any ideas, methods, instructions or products referred to in the content.